SPACE TELESCOPE SCIENCE INSTITUTE
Operated for NASA by AURA

WFC3 Instrument Science Report 2011-10

Interpixel Capacitance in the IR Channel: Measurements Made On Orbit

B. Hilbert and P. McCullough
April 21, 2011

ABSTRACT

Using high signal-to-noise pixels in dark current observations, the magnitude of the inter-pixel capacitance (IPC) has been calcucated for the IR channel of WFC3. While the measured IPC magnitude of 6.3% is within 1σ of the value quoted in past reports (Brown, 2008), this work also documents the difference in IPC magnitude in each of the 8 pixels surrounding a central, single pixel source. This document details the test procedure used to measure the IPC and the results, and explains possibilities for correcting users' data.

Introduction

Inter-pixel capacitance (IPC) is a form of crosstalk present in many near-IR array detectors (it does not affect CCDs). A small fraction of the charge collected by an individual pixel during an exposure will be measured in the pixel's nearest neighbors during the readout of the detector. The IPC effect spatially smooths the distribution of charges on the detector, causing effects such as cosmic rays and hot pixels to affect a larger population of pixels than they would otherwise. For example, Figure 1 shows an area of the detector containing several hot pixels. Prior to the removal of IPC effects, each hot pixel caused elevated signal levels in its four nearest neighbors. The spreading of the signal also artificially decreases the Poisson noise values of flat-field sources, which can lead to an erroneously high value for the instrument's conversion gain factor (e^-/ADU), and therefore artificially high values of detected photons (McCullough et al. 2008).

The effects of IPC are visually similar to those of charge diffusion, although the mechanism responsible is different. While IPC is a form of crosstalk, charge diffusion occurs when electrons in the detector migrate to adjcent pixels while on their way through the detector. Since different wavelengths of light preferentially create charges at different depths within the detector,

charge diffusion should have a wavelength dependence, while IPC does not. Since charge diffusion affects only photo-generated signal, while this study relied on dark current signal, our results should not be contaminated by charge diffusion.

In this work, we use WFC3/IR data to directly measure the magnitude of the IPC, and we also confirm IPC levels and remove IPC effects using the method and deconvolution script given by McCullough (2008). Through multiple applications of the deconvolution strategy, we attempt to identify the deconvolution kernel needed to effectively remove IPC effects from IR channel data. Further details on the deconvolution method, along with an IDL script for performing the deconvolution, are described in the Analysis section, and presented in McCullough (2008).

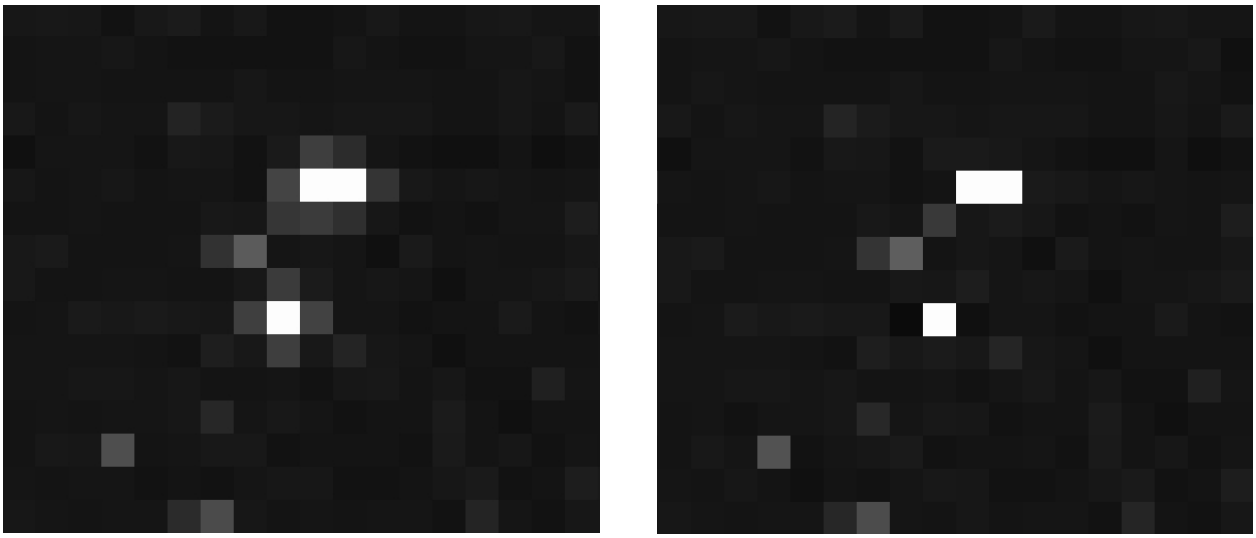

Figure 1: *The left panel shows several hot pixels in an IR channel image. IPC effects are apparent in the halo of warm pixels surrounding each of the hot pixels. The panel on the right shows the same data after IPC effects have been removed through deconvolution. Note the disappearance of the halos.*

Data

In order to isolate IPC effects, sources needed to be individual high-signal pixels surrounded by low-signal pixels. This would allow for the most accurate measurement of the amount of signal spreading from a central pixel to its neighbors. As a result, we chose to use dark current reference files for this measurement. The majority of hot pixels within the dark current frames were isolated from one another and the large number of individual ramps that were combined to form the reference files ensured the best possible signal-to-noise values despite the low signal levels.

We performed the primary analysis on the SPARS200 full-frame dark current reference file *u4819494i_drk.fits*. This ramp was created by averaging together 25 individual SPARS200 dark current ramps collected in SMOV and Cycle 17. In addition to the noise reduction associated with combining the 25 ramps, the long exposure time (2803 seconds) of the SPARS200 sample

sequence maximized the signal collected in each ramp. Results were confirmed using the dark current reference files for the SPARS100, STEP200 and STEP400 sample sequences (*u4819491i_drk.fits*, *u481949mi_drk.fits*, and *u481949ti_drk.fits*). In addition to having a high signal to noise ratio, the dark current reference files also had the advantage of being created with the calwf3-processed *ima* versions of the dark current ramps. This means that reference pixel subtraction had been performed in order to remove the bias level and any bias drift from the data, and the zeroth read had been subtracted from all subsequent reads, removing pixel-to-pixel variations in the zero level from the data.

For the remainder of this report, we refer to pixels immediately adjacent to a central hot pixel using the common directional terms "above", "below", "left" and "right. These terms are independent of quadrant and read out direction, and instead given relative to the detector orientation used in other ground testing and on-orbit analyses. Figure 2 shows this detector orientation, with the circular dark spot of the so-called "death star" located along the bottom edge of the detector, and the more diffuse "wagon wheel" feature located in the lower right corner.

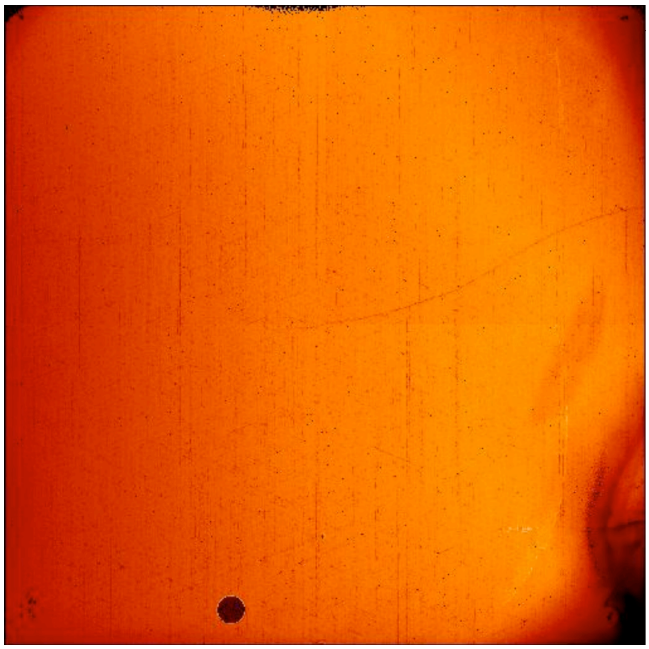

Figure 2: *Flat field image from the WFC3/IR channel, for the purpose of displaying the detector orientation refered to in this analysis.*

Analysis

We used two independent methods to measure the magnitude of the IPC in WFC3/IR data. The first was a direct measurement of the excess flux in the pixels surrounding hot pixels in the dark current data described above. The second method involved using the directly measured IPC values in a deconvolution script designed to remove IPC effects from data. By comparing the

residual signals after the deconvolution to background levels in the data, we were able to confirm the accuracy of the directly measured results.

Direct Measurement

The most straight forward way to determine the level of IPC was through the direct measurement of excess flux around hot pixels. First, we identified all pixels that had a signal rate at or above 0.17 DN/sec (0.40 e^-/sec) in the final read of the *ima* file. In order to prevent contamination from nearby hot pixels, if a second hot pixel appeared anywhere inside of a 5x5 pixel box centered on a given hot pixel, both were excluded from the analysis.

The resulting 5,178 members of this population of isolated hot pixels in the SPARS200 dark reference file next had background levels subtracted. The local background signal for each hot pixel was calculated as the sigma-clipped mean in a 40x40 pixel box centered on the hot pixel. We then extracted a 3x3 pixel box centered around the hot pixel and subtracted the background signal from each of the 9 pixels in the box. Signal levels in the 3x3 box were then normalized by dividing the signal in each pixel by the sum of the signal in all 9 pixels. Once these steps were completed for all hot pixels, we had 5,178 3x3 pixel arrays from which to measure the magnitude of the IPC.

The top panel of Figure 3 shows a plot of the normalized signal in the pixel immediately above the hot pixel through the entire stack of hot pixels. The normalized signal is plotted against the measured signal (in DN) for the central, hot pixel. The black points show the normalized signal for the entire population of pixels. We also calculated the mean of the black points in a series of 1,000 DN wide bins and plotted those means as the green points. Finally, we calculated a best-fit line to all of the black points with central pixel signal levels of 7,000 DN or greater, which is shown in red. The bottom panel shows a similar plot, but made for all of the central, hot pixels. Notice that in this lower panel, the normalized signal fractions are mostly in the 90 – 100% range, versus the 0 – 5% range in the top panel. If IPC were not present, points in the lower panel would be centered around 100% and those in the top panel would be centered around 0%.

There are several features to note in these plots. First, in the upper panel there are a number of points located above the main population at low central pixel signal levels (x-values). These come about because of situations where the pixel located immediately above the central, hot pixel has an elevated dark current level, but not quite elevated enough to be caught by the filter put in place to assure that a given hot pixel was isolated. The slightly elevated dark current in this pixel then causes this pixel to contain a significantly larger fraction of the total flux in the 3x3 pixel box than in the case of a pixel with average dark current.

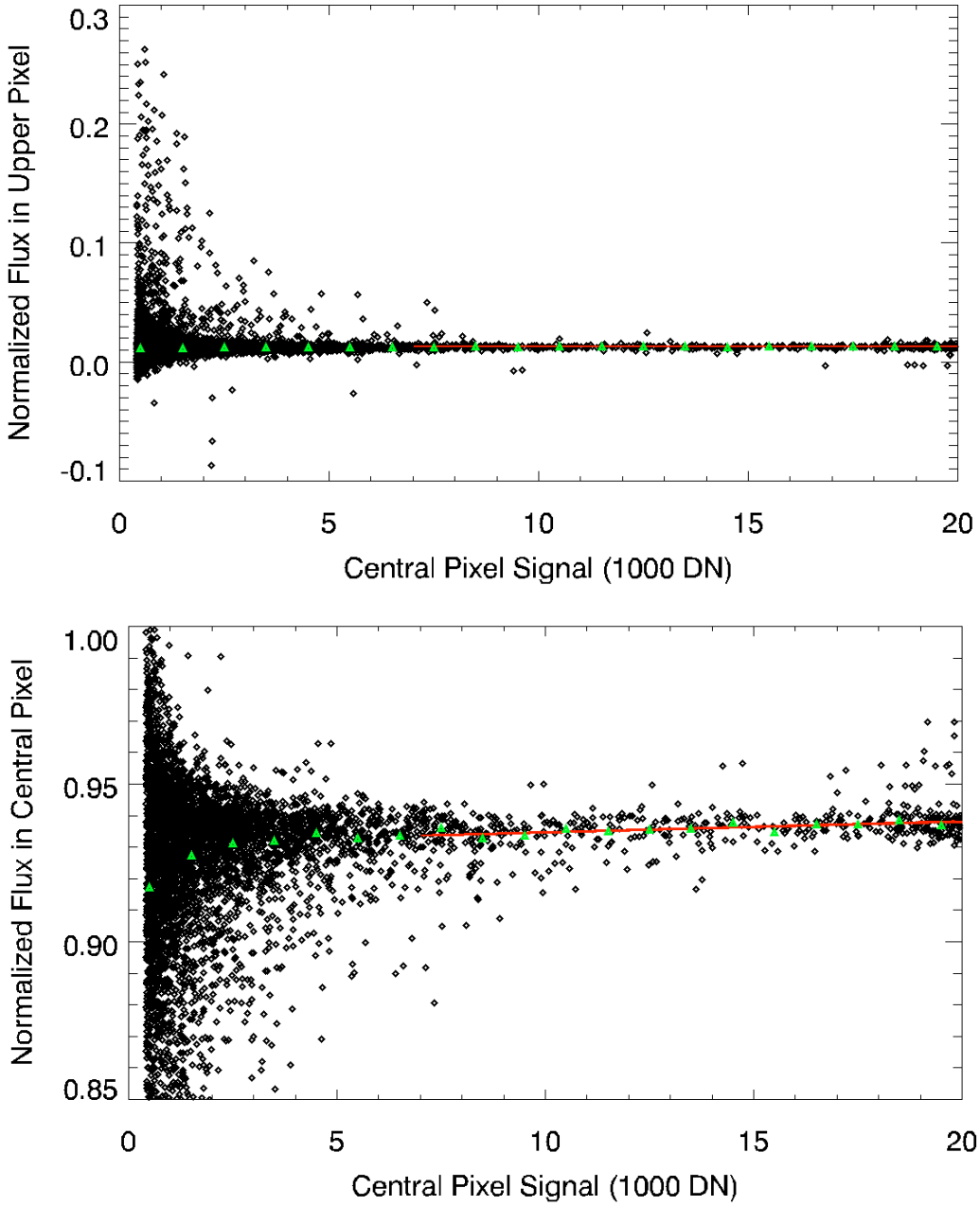

Figure 3:

(Top panel) *Normalized signals in the pixels immediately above the hot pixels versus the measured singal in the central, hot pixels (black points). As the central pixels become hotter, the fraction of signal measured in the pixels above settles to a constant value. The green points represent the sigma-clipped mean values calculated when the black points are grouped into bins with a width of 1,000 DN. The red line is a best-fit line to the black data points, but only for hot pixels with signal levels over 7,000 DN, the purpose of which was to search for any signal level dependence of the normalized level.*

(Bottom panel) *The same plot, but made for the central, hot pixels.*

For example, imagine the case where the central hot pixel has a signal of 1,000 DN. Now imagine that the pixel immediately above the hot pixel has a dark current of 0.1 DN/sec, rather than the nominal value of 0.02 DN/sec (Hilbert and McCullough 2010). For the final read in a SPARS200 exposure (2,803 second exposure time) this implies that the upper pixel has a signal of 280 DN due to dark current. The background subtraction step will remove 56 DN of this signal, assuming that the background is equal to the signal generated by the nominal dark rate of 0.02 DN/sec. This leaves 224 DN in the upper pixel. Assuming the other 7 pixels surrounding the central pixel have nominal dark current rates, the background subtraction should remove all dark current-generated signal from them, leaving behind only IPC-generated signal. Approximating IPC as a 1.5% effect on each of the 4 pixels immediately adjacent to the hot pixel (totaling 6%, which is the value used in Brown 2008), we expect IPC to add (1,000. * 1.5%) 15 DN to each of these 4 pixels, including the upper pixel. Performing the normalization step described above, we see in Equation 1 below that the upper pixel with its slightly elevated dark current will contain 18.6% of the total flux in its 3x3 pixel box. This corresponds to a y-value of 0.186 for an x-value of 1,000 in the top panel of Figure 3. This is well above the main population of black points, showing that contamination due to elevated dark current can have an effect on the measured IPC value.

$$\frac{224+15}{1000+(4*15)+224} = 0.186 \quad (1$$

In fact, our initial calculation of IPC was performed simply by summing the signal values through the stack of 3x3 boxes for each of the 9 pixels, thereby creating a "super" 3x3 pixel box, which was then normalized. In effect, this method calculated the weighted mean signal in each of the 9 pixels, where the hot pixels were given more weight than the cooler pixels. However, this weighting scheme meant that those pixels described above, which were contamined by a warm-but-not-hot neighboring pixel, had a significant contribution to the final super 3x3 pixel box. Using this method, the calculated IPC values were higher by about 0.001 than those calculated via our final method which, as detailed below, is an almost 1-σ effect.

The same effect also causes a decrease in the mean normalized flux levels (green points) with decreasing signal levels in the central hot pixel (lower panel of Figure 3). As described above, in the case where one or more of the 8 surrounding pixels is somewhat hot, but not hot enough to be flagged as a hot pixel, then the surrounding pixels will contain an abnormally high fraction of the total signal in the 3x3 pixel box. Or as is seen in the lower panel, the central pixel will contain an abnormally low fraction of the total signal. As the signal level in the central pixel decreases (ie moving to the left on the plot), the threshold of the signal rate needed to produce this effect decreases and the situation becomes more common.

Finally, we use the best-fit line to the higher signal levels (in red) in order to check for any trends in the normalized signal rate. We limited the range of the line-fitting to points with signal levels higher than 7,000 DN in order to avoid the low normalized signal levels (green points) described above. This reduced the number of 3x3 pixel boxes used in our analysis from 5,178 to

575. We fit the lines using IDL's robust_linefit.pro, which rejects outliers before fitting. We were most concerned with confirming a best fit slope of essentially zero.

With all slopes very close to zero (results are shown in Table 1 and translate to a variation in IPC of no more than 0.001 for the signal range in Figure 4), we then calculated the value of the IPC as the sigma-clipped mean value of the same points used in the line-fitting. The uncertainty associated with the IPC value was calcuated as the robust standard deviation of these same points. Further analysis of the slopes and the variations they imply suggests that a spatial dependence on the IPC across the detector may be the cause. Details are discussed in the IPC Variation section below.

-27	21	-5.1
-33	580	-58
-22	4.2	1.8

Table 1: *Slopes of the best-fit lines shown in red in Figure 4. The slopes in this table have been divided by* $1x10^{-9}$ *for clarity. The largest slope (excluding that for the central pixel), implies a change in mean IPC level of 0.0011 between the low and high signal ends of Figure 4. This is comparable to the calculated uncertainties presented in Table 2.*

With our measurement method defined and assured of no large variation in IPC value with signal level, we performed the calculations separately for each of the 9 pixels in the stack of 3x3 pixel boxes collected in our hot pixel search. Table 2 shows the results of the calculations on the SPARS200 dark current reference file, with the 9 cells of the table corresponding to the 9 pixels in the 3x3 box. We find that the magnitude of the IPC is identical in the pixels above and below the central hot pixel. The IPC values in the pixels to the left and right of the central pixel are also identical, but have a different value than that in the above/below pixels. Figure 4 shows plots similar to those seen in Figure 3 for each of the nine pixels, and with plot ranges narrowed to help clearly show the measured IPC magnitude. We have also omitted the green points from these plots for clarity.

0.0011 +/- 0.0006	0.0127 +/- 0.0009	0.0011+/- 0.0006
0.0163 +/- 0.0014	0.936 +/- 0.0045	0.0164 +/- 0.0011
0.0011 +/- 0.0006	0.0127 +/- 0.0010	0.0011 +/- 0.0006

Table 2: *IPC values and uncertainties for the pixels in a 3x3 box centered on a hot pixel, calculated using the direct measurement method on the SPARS200 dark current reference file. Summing the values in the 8 non-central pixels, we see that 0.063, or 6.3% of the flux in a single pixel source is measured in the surrounding 8 pixels, with an uncertainty of 0.7%. Values calculated using several other long-exposure dark current reference files were identical to well within the uncertainties.*

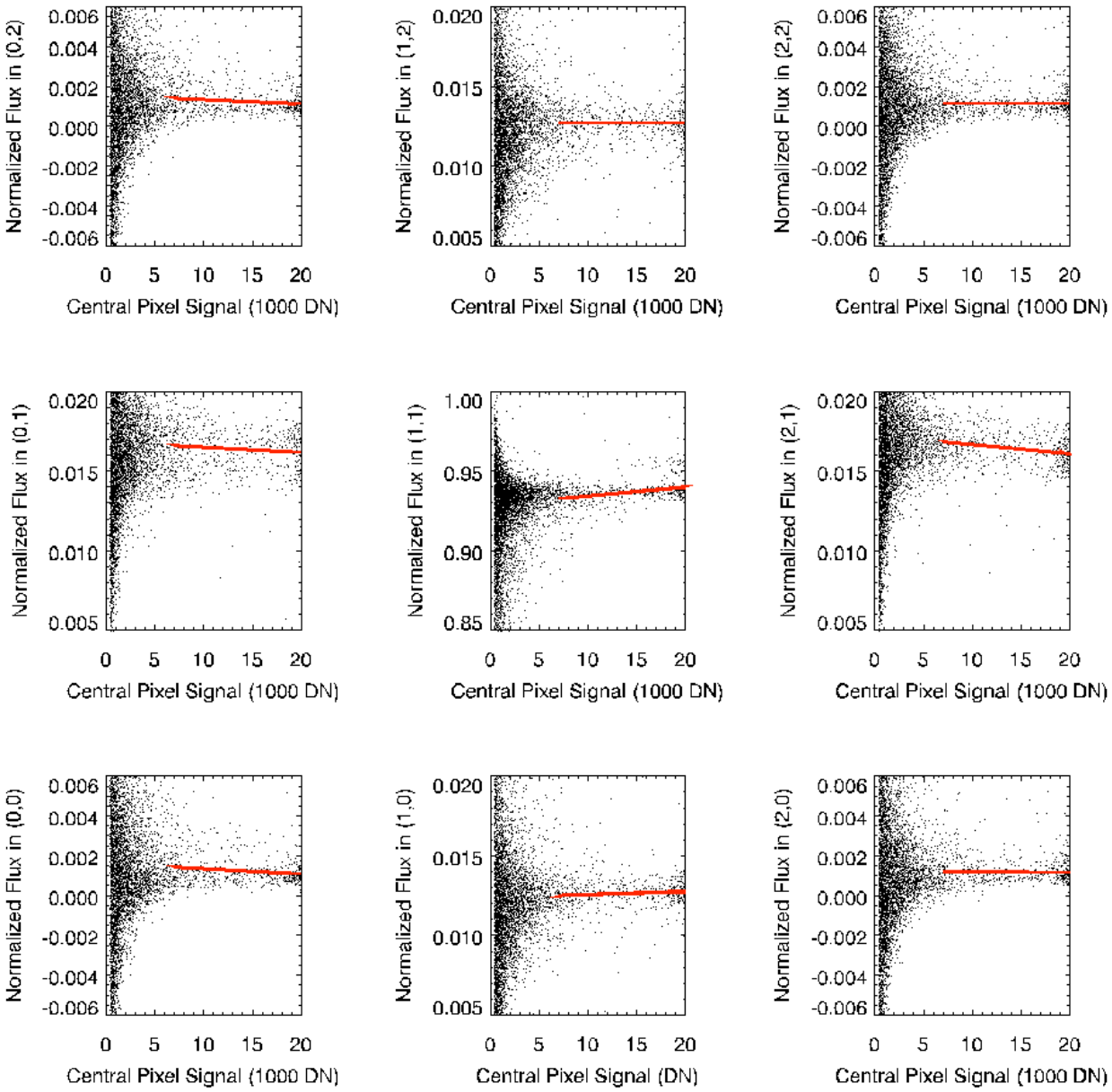

Figure 4: *Normalized signal values in each of the 9 pixels in the stack of 3x3 pixel boxes extracted during the hot pixel search. The central plot shows the normalized signal in the central hot pixels. Significant, non-zero signals are seen in the 4 pixels adjacent to the central pixel, revealing the presence of inter-pixel capacitance. The four corner pixels, which share only a corner in common with the central pixel, show normalized signal values that are above zero. The IPC values and uncertainties associated with these plots are listed in Table 2 and represent the sigma-clipped mean and standard deviations of the points with signals above 7,000 DN.*

We repeated the calculations for the STEP400, STEP200 and SPARS100 dark current reference files, as these sample sequences have the four longest exposure times in the IR channel. For all ramps, the calculated IPC values match those given in Table 2 to better than 0.0003, which is a factor of 3-4 smaller than the uncertainties listed in the table. Measured

uncertainties also matched those seen in Table 2. Since we are (largely) measuring the same set of hot pixels in the four ramps, this implies that a given pixel's behavior with respect to IPC is relatively stable from ramp to ramp. Further supporting this conclusion is that each dark current reference file produced very similar plots to those seen in Figure 4.

Note that summing the values in all 9 pixels results in a total normalized flux of 0.9985. The remaining 0.15% is comparable to the signal measured in one of the 4 corner pixels and also the uncertainty in the 4 adjacent pixels.

A more thorough examination of spatial variation in IPC level on a HgCdTe device very similar to that in the IR channel was conducted by Seshadri et al. (2008). Their results, based on measuring IPC by resetting individual pixels to various voltage levels, are similar to our values in Table 2. They find IPC values between 1.4% and 1.55% in the four adjacent pixels, and 0.13% in the corner pixels. In addition, histograms of the IPC levels for all pixels on their HgCdTe detector reveal a full width at half maximum (FWHM) of 0.12% for the population of each of the four adjacent pixels. This value is also very similar to our reported uncertainties of 0.09% - 0.14% for the same four pixels.

Deconvolution

In order to confirm the validity of the IPC values calculated directly from the hot pixels we input these values into an IPC correction script and examined the results. Our first test was to apply the correction to the final read of the SPARS200 dark current reference file, which was the data used to generate the IPC values. This step acted as a test of the efficacy of the correction script itself.

If the IPC values measured above were correct and the correction script was successful, we expected to see the elevated flux in the four pixels immediately adjacent to the central pixel (the script does not apply a correction to the four corner pixels) return to the central pixel, leaving the signals in the four adjacent pixels identical to the background signal levels.

Past studies have modeled IPC-affected data as a convolution of IPC-free data with a small kernel (Finger et al. 2005). McCullough (2008) presents a strategy for the removal of IPC effects using deconvolution with a 3x3 pixel kernel, where each element in the kernel contains the normalized fraction of measured signal associated with a single pixel source located in the central pixel. An example kernel is shown in Equation 2. He also argues that this IPC removal strategy can be recast as a convolution with a 3x3 pixel kernel where the 8 non-central coefficients are replaced by their own negative values, while the central coefficient then becomes $1+\alpha+\beta+\gamma+\delta$. As the script provided in McCullough (2008) uses the deconvolution strategy, we followed that method for this analysis. The two methods are mathematically equivalent to a very good approximation.

In order to remove IPC-created signal, we used a slightly modified version of the deconvolution script. This script deconvolves a user-supplied 3x3 element kernel from an input data array. Each element in the 3x3 array contains the fraction of flux in that pixel, assuming that the central pixel is the location of the source. The total summed value of all 9 elements is 1.0. Equation 2 shows the form of the kernel.

$$k = \begin{bmatrix} 0 & \gamma & 0 \\ \alpha & 1.0 - (\alpha + \beta + \gamma + \delta) & \beta \\ 0 & \delta & 0 \end{bmatrix} \quad (2$$

The deconvolution script assumes that no charge from the central pixel is measured in any of the four corner pixels, which is why these pixels have values of zero in Equation 2. The original version of the script forced α and β to contain identical values. Similarly, γ and δ were forced to contain the same value (which could be different from the α/β value). We modified the script so that four separate non-zero values could be entered for the 4 elements. This way, we could check for any left neighbor vs right neighbor and above neighbor vs below neighbor dependence of the IPC.

We used the values in Table 2 for α, β, γ, and δ, ran the deconvolution script, and then repeated the analysis described in the Direct Measurement section on the now IPC-corrected data. As a local background subtraction was one of the steps in the analysis, we expected to see normalized signal levels consistent with zero in the corrected data. This would mean that the pixels surrounding the hot pixels had been corrected to the point that their remaning signal was equal to the local background level.

Figure 5 is identical to Figure 4 but created using the IPC-corrected data. The plots for the four corner pixels are identical in both figures, as expected. The plots for the four pixels adjacent to the central pixel are very similar in shape in both figures, but in Figure 5 we see that the normalized flux levels are now centered on zero, rather than the 1.27% and 1.64% seen in Figure 4. Table 3 shows the "IPC" values calculated for the IPC-corrected data and as expected, the signals in the four corrected pixels are consistent with zero, while the normalized flux in the central pixel is now shy of 100% by 0.65%, due in large part to the four uncorrected corner pixels.

0.0012 +/- 0.0006	0.00004 +/- 0.0009	0.0012+/- 0.0006
0.0001 +/- 0.0016	0.993499 +/- 0.0057	0.0001 +/- 0.0013
0.0012 +/- 0.0006	0.000006 +/- 0.0013	0.0012 +/- 0.0006

Table 3: *IPC values and uncertainties calculated using the IPC corrected SPARS200 dark current reference file. The values in the four pixels directly adjacent to the central pixel are all consistent with zero, indicating that the IPC correction script was successful. Also note that the fraction of flux contained in the central pixel is now below 1.0 by roughly the combined value of the four uncorrected corner pixels.*

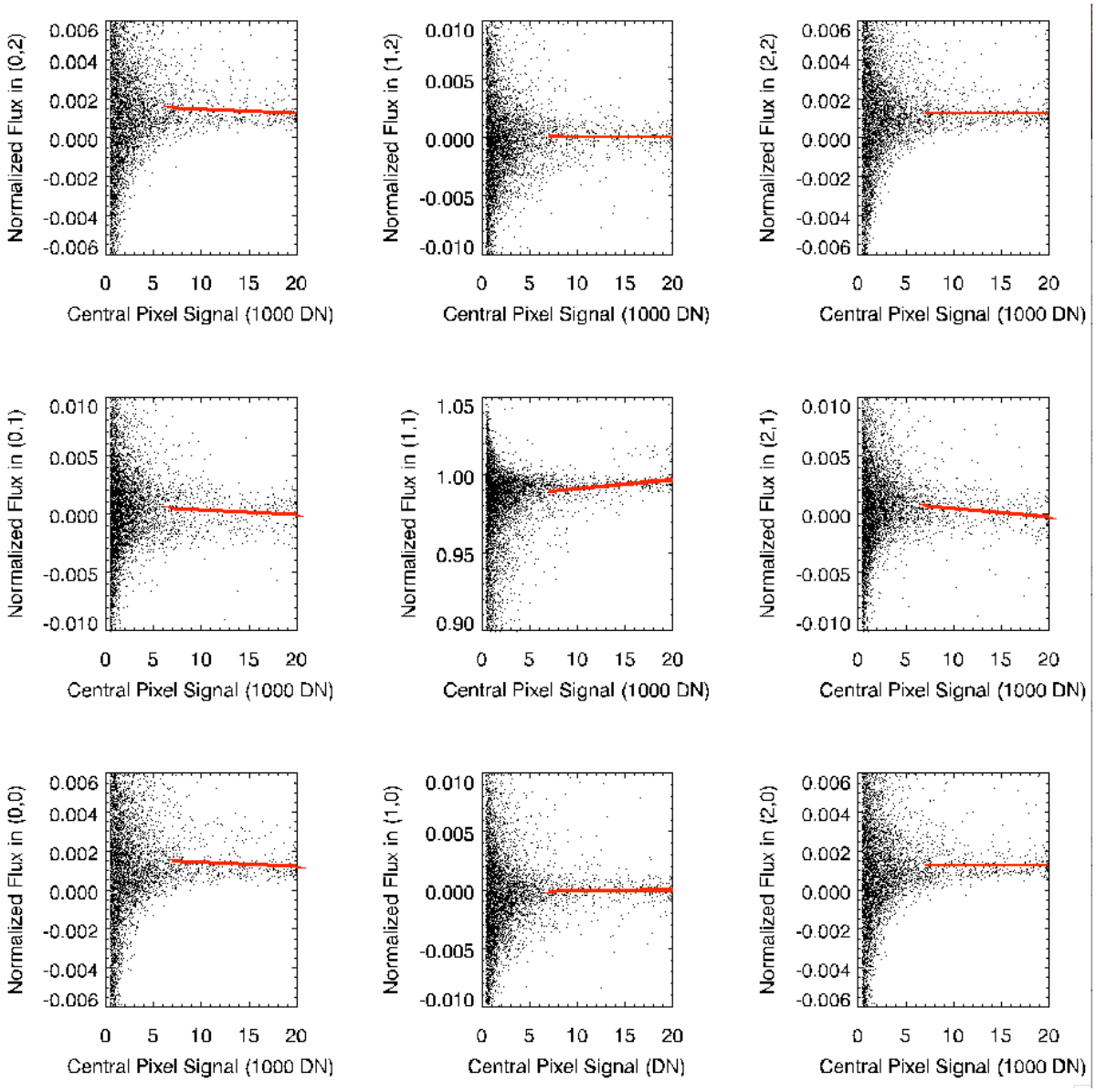

Figure 5: *The same plots as seen in Figure 4, but after IPC effects have been removed from the SPARS200 data. The four corner pixels are not corrected by the deconvolution script and are therefore identical to the uncorrected case. The four pixels adjacent to the central pixel now show normalizd flux values consistent with zero, implying a successful removal of IPC effects. The central pixel now contains very close to 100% of the signal. See Table 3 for mean values. Note that since we corrected all pixels with the single kernel, the vertical spread of the corrected points is very similar to that of the uncorrected points. This is why the uncertainties in the corrected and uncorrected cases are the same, as seen in Tables 2 and 3.*

Spatial Variations

Once we had confirmed that the direct measurement method was capable of producing accurate measurements of the IPC level of the detector, we used the results from this method to search for spatial and temporal variations in the IPC.

First, we searched for any signs of a spatial dependence of the IPC across the detector. Using only the high signal measurements (central hot pixels with signal above 7,000 DN) used to calculate the IPC values in Table 4, we plotted the normalized flux values of the corrected data versus distance from the amplifiers, which are located in the corners of the detector. Each quadrant of the detector is read out through the amplifier in the nearest corner.

Since our IPC correction used a single set of values across the detector, the overall magnitude of the normalized signal will shift downward after correction, but the spread in the corrected and uncorrected data will remain the same, as seen by the identical uncertainty values in Tables 2 and 3, as well as the very similar appearances of the plots in Figures 4 and 5. Therefore, after correcting the data with the IPC values in Table 2, remaining large scale patterns in the data will be variations in signal due to differences in the IPC behavior across the detector.

Unlike in the analysis described prior to this point, in Figure 6 we show the behavior of the IPC across the detector in relation to the readout direction of the detector. Since this direction varies, in an absolute sense, from quadrant to quadrant, in Figure 6 we redefined the 4 adjacent pixels. Rather than the absolute "left", "right", "up", and "down" used previously, in Figure 6 we describe the 4 adjacent pixels relative to the central hot pixel as being in the "column closer to the amplifier", "column farther from the amplifier", "row closer to the amplifier" and "row farther from the amplifier". Another way to think of these directions is "upstream" and "downstream" from the central pixel. The signal from the two pixels in the row and column closer to the amplifier will reach the amplifier before the signal from the central pixel, and therefore can be thought of as "downstream" from the central pixel. Similarly, the pixels farther from the amplifier than the central pixel can be pictured as "upstream". With the amplifiers in the four corners of the detector, the "upstream" direction is toward the center of the detector, and the "downstream" direction is toward the corners.

In Figure 6, the red and purple lines represent the two "upstream" pixels (purple is for the pixel in the column farther from the amplifier, while red is for the pixel in the row farther from the amplifier), while the blue and yellow lines represent the "downstream" pixels (blue is for the column closer to the amplifier, while yellow is for the row closer to the amplifier).

In these plots, the colored lines show the best-fit lines to the normalized signal values. In quadrant 3, the points used in the line-fitting are represented with large diamonds, in order to be better show the distribution of values that went into the line-fitting. In the other three quadrants, the points are left as small dots, in order to make the best-fit lines more visible.

After dividing up our initial set of 575 hot pixels by quadrant, we had between 130 and 180 measurements per pixel position per quadrant. Uncertainties in the slopes associated with the line fitting indicate that the measured slopes are significant. For the red and blue lines, the uncertainties on the slopes are factors of 5-6 less than the slopes themselves. For the purple and yellow lines with their much smaller slopes, the uncertainties are 50-100% of the slope values.

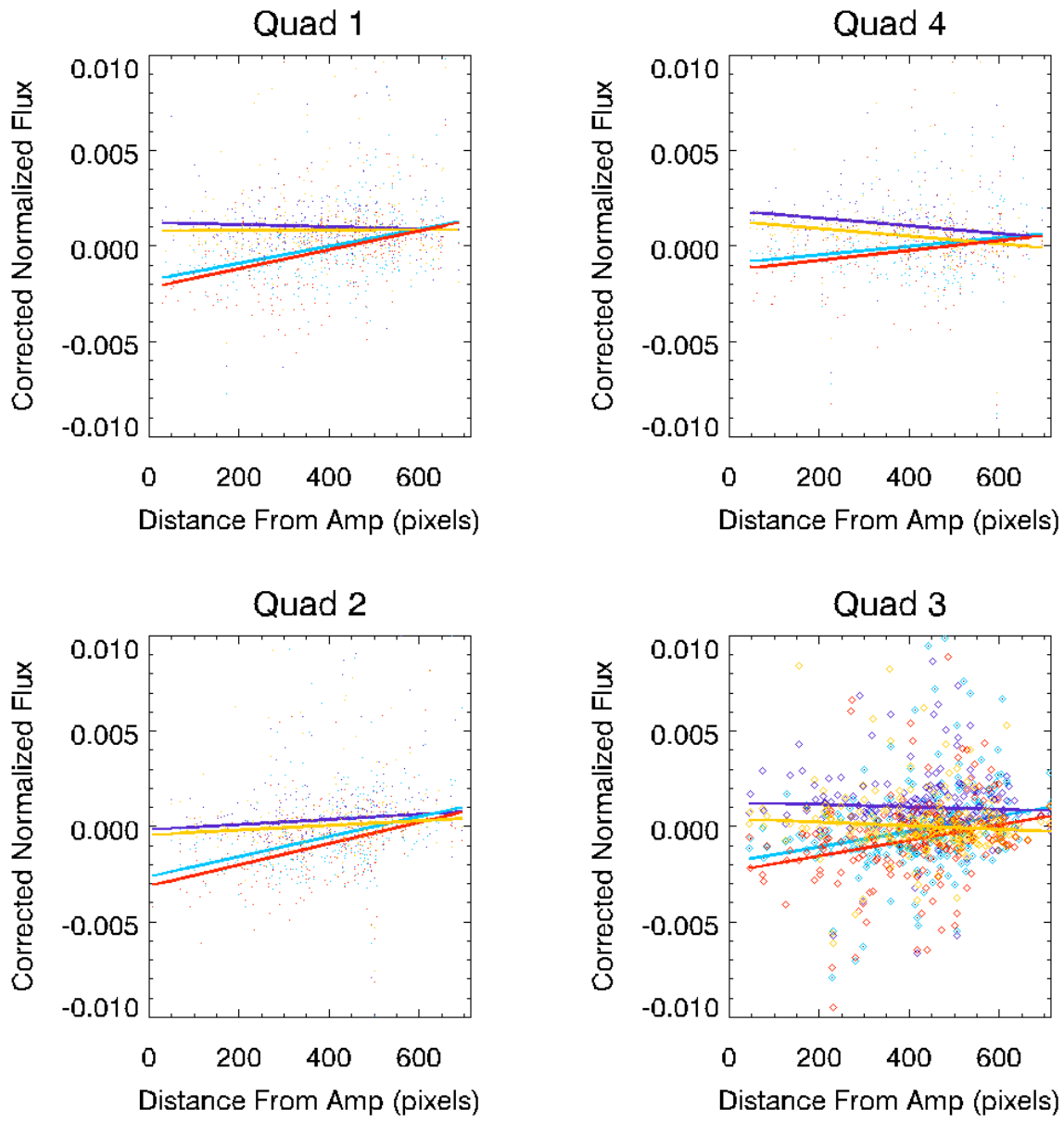

Figure 6: *Plots of normalized signal versus detector position for each quadrant, the four lines represent the 4 pixels adjacent to the central pixel according to direction relative to the readout amplifier. The purple and red lines show the signal levels for the pixels in the column and row "upstream" from the central pixel, respectively. The blue and yellow lines show the signal levels for the pixels in the "downstream" column and row, respectively. Note that the largest variations in signal level are approximately 0.0025 between the pixels closest and farthest from the amplifier.*

Figure 6 shows that the variation in normalized signal across a quadrant can be as much as 0.0025, which agrees with the values of the listed uncertainties in Table 2 (as those are standard deviation values and here we are calculating the total variation from one end to the other). Curiously, the two "upstream" pixels (purple and red lines) behave differently from one another, as do the two "downstream" pixels. In fact, Figure 6 shows results which are opposite to those

expected. The two pairs of similarly behaving pixels are each composed of one "upstream" and one "downstream" pixel. The cause behind this behavior is unknown.

The magnitudes of the best-fit line slopes imply that at worst the IPC correction, as implemented in this analysis, will fail to move approximately 1.1% (4 corner pixels each at 0.12% plus a total of approximately 0.6% from locations at small distances from the amplifier in quadrant 2) of the signal back into the central pixel where it should be. In most positions on the detector this value will be lower, reaching a minimum of roughly 0.5% (due to the 4 uncorrected corner pixels) in the center of the detector, where the correction of the 4 adjacent pixels is best. Future IPC studies utilizing more data may wish to more carefully characterize the IPC level across the detector, in order to create a more accurate, spatially-dependent correction.

As mentioned previously Seshadri et al. (2008) created a map of IPC for their detector. Histograms of the IPC values for their detector showed FWHM of 0.12% for the four pixels adjacent to the center pixel. This value is very similar to our stated uncertainties, implying that the our observed IPC spatial variations are real. Figure 10 in Seshadri et al. shows a plot of row-averaged IPC level, which appears to vary in a linear fashion by roughly 0.1% across a span of almost 1000 columns. This is comparable to our measured variations of up to 0.25% across the 717 pixel distance across the diagonal of each quadrant. Our measurements were also made using only 130-180 hot pixels per quadrant, implying a much less complete picture of IPC variation than that presented by Seshadri et al. In order to generate a more complete IPC map for the IR channel, a future study would need to mimic the strategy used by Seshadri et al., where populations of pixels are reset to various voltages. If this is not possible, IPC could be calculated with enough data by examining cosmic rays, although in this case, charge diffusion effects would contaminate IPC measurements.

Temporal Variations

Finally, we collected all of the SPARS200 dark current observations made as part of the dark current calibration programs in observing cycles 17 and 18. This resulted in a total of 49 dark current observations, which are listed in Table 5 in the Appendix. As with the calculations performed on the dark current reference file, we used the final read of each of these 49 files in order to have an image with the maximum signal-to-noise. We calculated IPC levels for each of the 49 files using the direct measurement method, in order to serch for variations in IPC over time. Figure 7 shows the measured IPC values for the 8 pixels surrounding the central hot pixels, for all 49 files, while Table 4 shows the mean and sigma-clipped standard deviations for these values. The mean values in Table 4 agree with those in Table 2, derived from the dark current reference file. The listed uncertainties are very small, indicating very stable IPC values over time. The reason that the uncertainties below are more than an order of magnitude less than those in Table 2 is because here the spatial variations in IPC are being ignored. We record IPC values for each of the 49 observations and look at the variation in those values, while ignoring the larger spatial variations that Figure 7 shows are present within each IPC value. By ignoring the spatial variations, we see that temporally the measured IPC is very repeatable. The plots in Figure 7 support this observation, showing no long-term IPC variation over the past ~20 months.

0.00109 +/- 0.00005	0.01259 +/- 0.00008	0.00109 +/- 0.00007
0.01629 +/- 0.00008	0.9366 +/- 0.0004	0.01629 +/- 0.00008
0.00112 +/- 0.00005	0.01259 +/- 0.00008	0.00105 +/- 0.00006

Table 4: *Means and sigma-clipped standard deviations for the IPC values calculated from a set of 49 SPARS200 files collected during Cycles 17 and 18.*

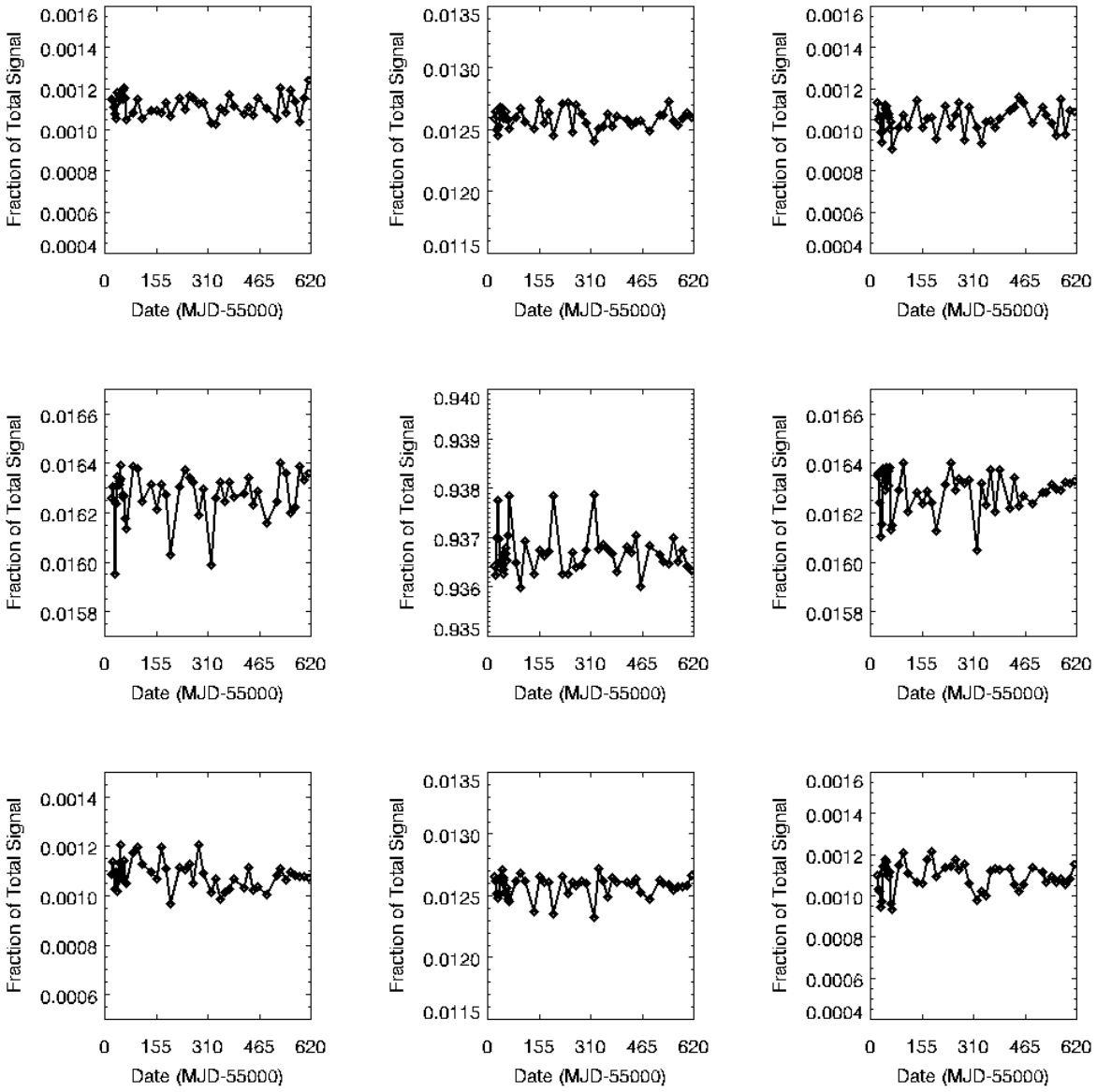

Figure 7: *IPC versus time from the final read of each of a set of 49 SPARS200 dark current observations. These plots show no long-term trend in IPC over time.*

Results

With spatial and signal level dependencies of the IPC at levels comparable to the measured uncertainties, we find that the results presented in Table 2 represent the best measurement of the IPC level in the IR channel. Summing the eight values in the pixels surrounding the central pixel, we find that IPC results in 6.3% of a pixel's flux being spread into its nearest neighbors (with an uncertainty of 0.7%). This matches the IPC correction factor previously used to correct the calculation of the conversion gain in the IR channel (Brown 2008; Hilbert 2007). An IPC effect of 6.3% will decrease the variance, which is used to calculate the gain, by twice that amount, or 12.6%. Therefore our calculated value is within 5% (and 1σ) of the value (12%) used in the two reports referenced above. We see suggestions of spatial variation of the IPC when compared to distance from the readout amplifiers. A more thorough search is needed to better characterize the variation. Conversely, we see no temporal variation in IPC levels.

Conclusions

We have used hot pixels in high signal-to-noise dark current data to directly measure the IPC of the WFC3/IR channel and we have confirmed that a previously described deconvolution method (McCullough 2008) effectively removes the IPC effects, with less than 1% of the total signal remaining uncorrected and spread across the 8 pixels surrounding a central source. Our results for the magnitude of the IPC are within 5% and 1σ of the total magnitude previously used in IPC corrections and also show that there is a significant difference between the magnitude of the IPC in the vertical versus the horizontal direction on the detector. By using the IDL script presented in McCullough (2008) and the kernel shown in Equation 2 with values from Table 2, users can remove IPC effects from their data.

By removing what is essentially a smoothing of the data, the IPC correction minimizes the population of pixels affected by hot pixels and cosmic rays, potentially leading to an improvement in photometry. As seen in Figure 1, after IPC correction a pixel with elevated dark current should affect only that pixel, rather than that pixel plus the four pixels immediately adjacent to it.

Ideally, IPC effects should be removed separately from the raw observations and the calibration data (dark current ramps, flat fields) prior to performing basic calibration steps. Currently, this correction is not present in the calwf3 data reduction pipeline and must therefore be done manually. See McCullough (2008) for more disussion on data reduction strategies involving IPC.

Acknowledgments

The author would like to thank Howard Bushouse for reviewing this document and providing many useful comments.

References

Brown, T., 2008, WFC3 ISR 2008-05. "***WFC3 TV3 Testing: IR Channel Blue Leaks***".

Finger, G., Beletic, J. W., Dorn, R., Meyer, M., Mehrgan, L., Moorwood, A. F. M., & Stegmeier, J. 2005, Experimental Astronomy, 19, 235.

Hilbert, B., 2007. WFC3 ISR 2007-28. "***WFC3 TV3 Testing: IR Gain Results***".

Hilbert, B. and McCullough, P., 2010. WFC3 ISR 2009-21. "***WFC3 SMOV Results: IR Channel Dark Current, Readnoise, and Background Signal***".

McCullough, P., 2008, WFC3 ISR 2008-26. "***Inter-pixel capacitance: prospects for deconvolution***".

McCullough, P., Regan, M., Bergeron, L., Lindsay, K., 2008. PASP 120:759-776. "***Quantum Efficiency and Quantum Yield of an HgCdTe Inrared Sensor Array***".

Seshadri, S., Cole, D.M., Hancock, B.R., and Smith, R.M., "*Mapping electrical crosstalk in pixelated sensor arrays*", Proc. SPIE Vol. 7021, 2008.

Appendix

Proposal Number	Filename
11447	iabz05xqq_ima.fits
	iabz06geq_ima.fits
	iabz07axq_ima.fits
	iabz08ojq_ima.fits
	iabz09edq_ima.fits
	iabz10ghq_ima.fits
	iabz11acq_ima.fits
	iabz12d4q_ima.fits
	iabz13lfq_ima.fits
	iabz14ljq_ima.fits
	iab15h7zq_ima.fits
	iabz16h4q_ima.fits
	iabz17q3q_ima.fits
	iabz18suq_ima.fits
	iabz19e2q_ima.fits
	iabz20djq_ima.fits
11929	ibcu07ykq_ima.fits
	ibcu0ldxq_ima.fits
	ibcu1lv1q_ima.fits
	ibcu1yi2q_ima.fits
	ibcu20djq_ima.fits

	ibcu2ldjq_ima.fits
	ibcu2ywtq_ima.fits
	ibcu33onq_ima.fits
	ibcu3lwmq_ima.fits
	ibcu3ywvq_ima.fits
	ibcu4lfmq_ima.fits
	ibcu4ydgq_ima.fits
	ibcu59fkq_ima.fits
	ibcu5ldbq_ima.fits
	ibcu5ydaq_ima.fits
	ibcu6lq3q_ima.fits
	ibcu6ydsq_ima.fits
	ibcu72buq_ima.fits
	ibcu7yxnq_ima.fits
	ibcu85v8q_ima.fits
	ibcu8ldzq_ima.fits
	ibcu8yd7q_ima.fits
	ibcu98b1q_ima.fits
	ibcu9ldzq_ima.fits
	ibcuabmaq_ima.fits
	ibcub1tyq_ima.fits
	ibcubecnq_ima.fits
12349	iblt15c6q_ima.fits
	iblt31bkq_ima.fits
	iblt47hbq_ima.fits
	iblt63chq_ima.fits
	iblt79bgq_ima.fits
	iblt95btq_ima.fits

Table 5: *List of SPARS200 dark current observations used to monitor the IPC level versus time.*